

Voltage-Controlled Deblocking of Magnetization Reversal in Thin Films by Tunable Domain Wall Interactions and Pinning Sites

Jonas Zehner, Ivan Soldatov, Sebastian Schneider, René Heller, Nasrin B. Khojasteh, Sandra Schiemenz, Sebastian Fähler, Kornelius Nielsch, Rudolf Schäfer, and Karin Leistner*

High energy efficiency of magnetic devices is crucial for applications such as data storage, computation, and actuation. Redox-based (magneto-ionic) voltage control of magnetism is a promising room-temperature pathway to improve energy efficiency. However, for ferromagnetic metals, the magneto-ionic effects studied so far require ultrathin films with tunable perpendicular magnetic anisotropy or nanoporous structures for appreciable effects. This paper reports a fully reversible, low voltage-induced collapse of coercivity and remanence by redox reactions in iron oxide/iron films with uniaxial in-plane anisotropy. In the initial iron oxide/iron films, Néel wall interactions stabilize a blocked state with high coercivity. During the voltage-triggered reduction of the iron oxide layer, in situ Kerr microscopy reveals inverse changes of coercivity and anisotropy, and a coarsening of the magnetic microstructure. These results confirm a magneto-ionic deblocking mechanism, which relies on changes of the Néel wall interactions, and of the microstructural domain-wall-pinning sites. With this approach, voltage-controlled 180° magnetization switching with high energy-efficiency is achieved. It opens up possibilities for developing magnetic devices programmable by ultralow power and for the reversible tuning of defect-controlled materials in general.

so far, mainly originates from the electric currents utilized to control the magnetic properties. A promising alternative for increasing the energy efficiency of magnetic devices is to control the magnetism by electric fields instead of electric currents. This possibility has triggered intense research into magnetoelectric materials, but much of this is restricted to low temperature and high voltage operation and/or complex layer synthesis.^[1]

More recently, magnetolectric approaches involving the voltage-gating of magnetic nanostructures via a dielectric oxide or an electrolyte were examined.^[1–3] In these approaches, ferro- and ferrimagnetic metals or oxides exhibiting Curie temperatures above room temperature can be used and often only few volts are required during gating. The modulation of magnetic properties in voltage-gated magnetic nanostructures is based on either voltage-induced capacitive charging or electrochemical (magneto-ionic) processes.^[2–4]

Voltage-induced capacitive charging of a ferromagnetic metal interface causes volatile changes in the surface electronic band structure that affect the intrinsic magnetic properties in just a few atomic layers.^[5–10] In contrast, magneto-ionic mechanisms involve voltage-induced ion migration and electrochemical reactions,^[2,3,11–13] and can therefore induce very large and nonvolatile magnetic property changes.^[12,14–18] As a

1. Introduction

Reducing the power consumption by magnetic devices used for data storage and computing processes, as well as in micro- and nanotechnological systems in general, is a significant global challenge. Energy loss in common magnetic systems,

J. Zehner, Dr. I. Soldatov, Dr. S. Schneider, S. Schiemenz, Dr. S. Fähler, Prof. K. Nielsch, Prof. R. Schäfer, Dr. K. Leistner
Leibniz IFW Dresden
Helmholtzstrasse 20
Dresden 01069, Germany
E-mail: k.leistner@ifw-dresden.de

 The ORCID identification number(s) for the author(s) of this article can be found under <https://doi.org/10.1002/aelm.202000406>.

© 2020 The Authors. Published by Wiley-VCH GmbH. This is an open access article under the terms of the Creative Commons Attribution License, which permits use, distribution and reproduction in any medium, provided the original work is properly cited.

J. Zehner, Prof. K. Nielsch, Prof. R. Schäfer, Dr. K. Leistner
Institute of Material Science
TU Dresden
Dresden 01062, Germany
Dr. R. Heller, N. B. Khojasteh
Helmholtz-Zentrum Dresden-Rossendorf e.V.
Bautzner Landstr. 400
Dresden 01328, Germany
Dr. S. Schneider
Dresden Center for Nanoanalysis (DCN)
Center for Advancing Electronics Dresden (cfaed)
TU Dresden
Dresden 01062, Germany

DOI: 10.1002/aelm.202000406

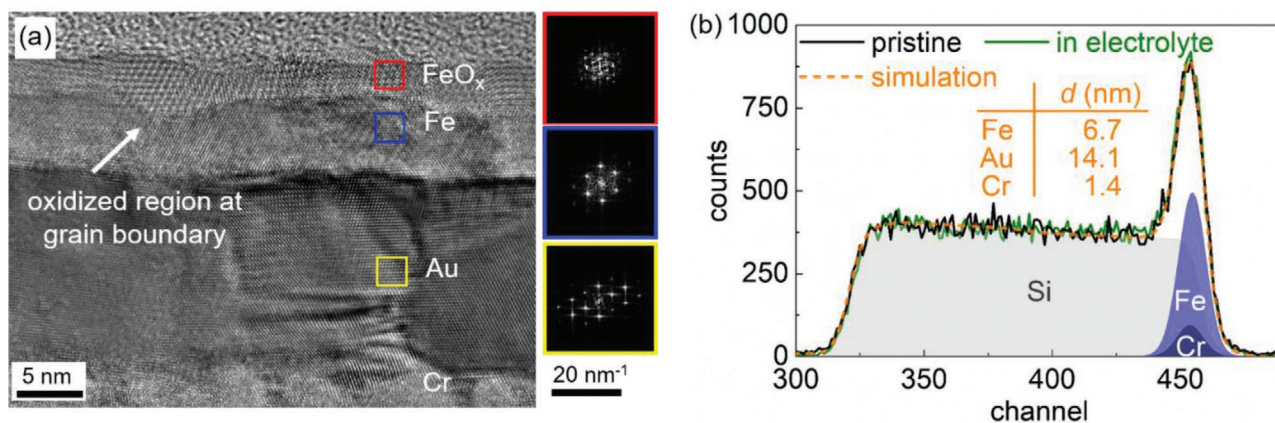


Figure 1. Layer architecture of pristine FeO_x/Fe thin films. a) Cross-sectional HR-TEM image and FFTs of the FeO_x/Fe/Au/Cr layers. b) RBS spectra, derived elemental contributions, and extracted layer thicknesses *d* for the layer in contact with air (black) and in the electrolyte (green). Also shown is the deconvolution of the simulated fit in the elemental subspectra, used to calculate the layer thickness. The fit is identical for both spectra, demonstrating that no change in thickness occurs upon addition of the electrolyte solution.

result, magneto-ionic materials have emerged as prominent energy-efficient candidates for voltage-programmable materials with potential applications in neuromorphic computing, domain-wall logic, magnetic random access memory, and magnet-based lab-on-a-chip technologies.^[3,12,14,19,20]

To date, studies on magneto-ionic effects in thin metal films have focused primarily on changes in the interface-perpendicular magnetic anisotropy (PMA)^[21–25] and the Dzyaloshinskii–Moriya interaction.^[26] There is growing recognition that voltage-induced changes in valency and phase, inherent to magneto-ionic effects, can be applied to the magnetic layer beyond the interface.^[13,17] For instance, voltage-control of magnetization up to ON/OFF switching of magnetism is possible in transition metal oxide (TMO)^[13,27] and hybrid TMO/metal films^[28–30] because of the switching between different chemical states induced by oxygen-, hydrogen-, or lithium-ion transport. In some cobalt-based oxides, due to high ionic diffusion coefficients, control of stoichiometry and phase transformations by reversible ionic mechanisms are achieved both at interfaces and beyond the ultrathin limit.^[31–34] For such materials, voltage-switching between antiferromagnetic and ferromagnetic or ferrimagnetic states is demonstrated.^[32,35] Further, studies on layered composites and nanoporous metal alloys indicate that also many other exciting magnetic phenomena, such as the exchange bias,^[14] spin reorientation,^[16,36] and the RKKY interaction^[37] length are tunable by electrolytic gating. Although films with uniaxial in-plane anisotropy hold great potential for switchable artificial magnetic stray field landscapes for lab-on-a-chip^[38] or for giant magnetoresistance sensors,^[39] there are no reports of magneto-ionic control of such films yet.

To exploit the full potential of the magneto-ionic voltage control of magnetism, it is essential to understand the underlying mechanisms. Until now, magneto-ionic effects have most often been explained solely in terms of integral voltage-dependent magnetization curves. Since the magnetization processes rely on the evolution of magnetic domains, the local magnetic microstructure is a decisive tool for understanding magneto-ionic effects. Until now, the modulation of domain expansion,^[12,26] domain contrast,^[25] and domain size^[40] after ionic modification of thin films have been reported. However, there

have been no reports of the direct and simultaneous detection of electrochemical oxidation/reduction reactions and changes in the magnetic domain structure.

In this study, we unravel the crucial role of magneto-ionic effects on the magnetic microstructure in FeO_x/Fe films with uniaxial in-plane magnetic anisotropy by combining in situ electrochemical, magnetization curve, and magnetic domain analysis. We demonstrate that low voltage-induced reduction/oxidation induces the reversible collapse of coercivity and remanence. In situ Raman spectroscopy revealed a phase transformation from iron oxide to iron, and vice versa, whereas in situ Kerr microscopy resolved that the decrease in coercivity upon reduction is concurrent with an increase in magnetic anisotropy and equilibrium-magnetic-domain size. As the origin, we propose a magnetic deblocking mechanism based on magneto-ionic changes of the Néel domain wall interactions and of the microstructural pinning sites. The control of magnetism via a tunable microstructure demonstrated in this study goes beyond conventional magneto-electric concepts since it exploits the extrinsic and not only the intrinsic film property changes. It opens up possibilities for developing magnetic devices programmable by ultralow power and for the reversible tuning of magnetic materials in general.

2. Results and Discussion

2.1. FeO_x/Fe Thin Films Display Uniaxial Anisotropy and Blocked Domain State

To investigate the role of the magnetic microstructure in magneto-ionic effects, we chose the FeO_x/Fe system, which is suitable for magneto-ionic manipulation.^[16] We prepared FeO_x/Fe films by oblique sputter deposition on Au/Cr/SiO₂/Si and subsequent native oxidation. Cross-sectional high-resolution transmission electron microscopy (HR-TEM) (Figure 1a) revealed that in the pristine state, the iron layer is polycrystalline with a lateral average grain size of about 30 nm (see also Figure S1 in the Supporting Information). A 2–3 nm thick native iron oxide layer was observed to form on top of the iron layer. Raman

spectroscopy identifies Fe_3O_4 as the dominant iron oxide phase (see Figure S2, Supporting Information), which is as expected after room temperature oxidation.^[41–43] The iron oxide follows the shape of the iron grains and penetrates deeper at the grain boundaries. The fast Fourier transformed (FFT) images of the individual layers (Figure 1a) show that the iron oxide-, iron-, and gold layers are all crystalline. The FFTs indicate that the individual iron grains align epitaxially with the underlying gold grains. This implies that the iron grains follow the orientation of the gold grains. Since the gold grains are oriented randomly in the film plane (see pole figures in Figure S3 in the Supporting Information), we assume that there is also no crystallographic in-plane texture for the iron grains.

The nominal thickness of the iron layer was determined by Rutherford backscattering spectrometry (RBS). Thin amorphous Si_3N_4 windows were used as substrate, because they allow the ion beam to penetrate the layer stack from the bottom side of the substrate.^[44] At a later stage, this enables the coupling with a liquid cell and in situ RBS measurements.^[44] Figure 1b shows the RBS spectrum and the derived contributions of Fe from the FeO_x/Fe layer, the Cr and the Au from the buffer layers, and the Si from the substrate. The individual layer thicknesses given in Figure 1b are calculated from the elemental areal densities. The evaluation of the areal density of Fe yields the nominal iron thickness as obtained by sputtering. The nominal iron thickness of 6.7 ± 0.5 nm, calculated from the RBS spectrum, matches the iron thickness of about 5 nm as observed in the HR-TEM images after native oxidation,

considering that about 1–2 nm of iron is “consumed” to form the iron oxide.

The FeO_x/Fe films exhibit an effective uniaxial magnetic anisotropy in the film plane, which arises primarily from geometric surface/grain shape effects connected to a self-shadowing effect during the oblique sputter deposition (see Figure S4, Supporting Information).^[45–48] Magnetization curves along the in-plane magnetic easy and hard axes were recorded by measuring the intensity in the Kerr micrographs at varying magnetic field (magneto-optical Kerr effect (MOKE) magnetometry) (Figure 2a).^[49] Along the easy axis, the shape of the curve is close to rectangular with a remanence ratio $M_R/M_S \approx 1$. The hysteresis loop along the hard axis is more rounded with $M_R/M_S \approx 0.75$ and coercivity $\mu_0 H_C$ comparable with the coercivity along the easy axis. This behavior deviates strongly from the linear hard-axis magnetization reversal (called “ideal” in the following) with zero remanence and coercivity by coherent rotation. The ideal linear behavior is known for Stoner-Wohlfarth single domain particles,^[50] and would also be expected in magnetic films if magnetic domains were not to be taken into account. In contrast, nonideal high-remanence hard-axis behavior in thin films is known to be caused by domain wall interactions,^[51] and it can be found in polycrystalline permalloy (FeNi)^[51–53] and cobalt^[54] thin films with uniaxial in-plane anisotropy.

The underlying magnetization and domain processes when applying the field along the hard axis are known and can be described as follows (Figure 2b).^[51] When the applied magnetic field is decreased from the saturated state (①), longitudinal

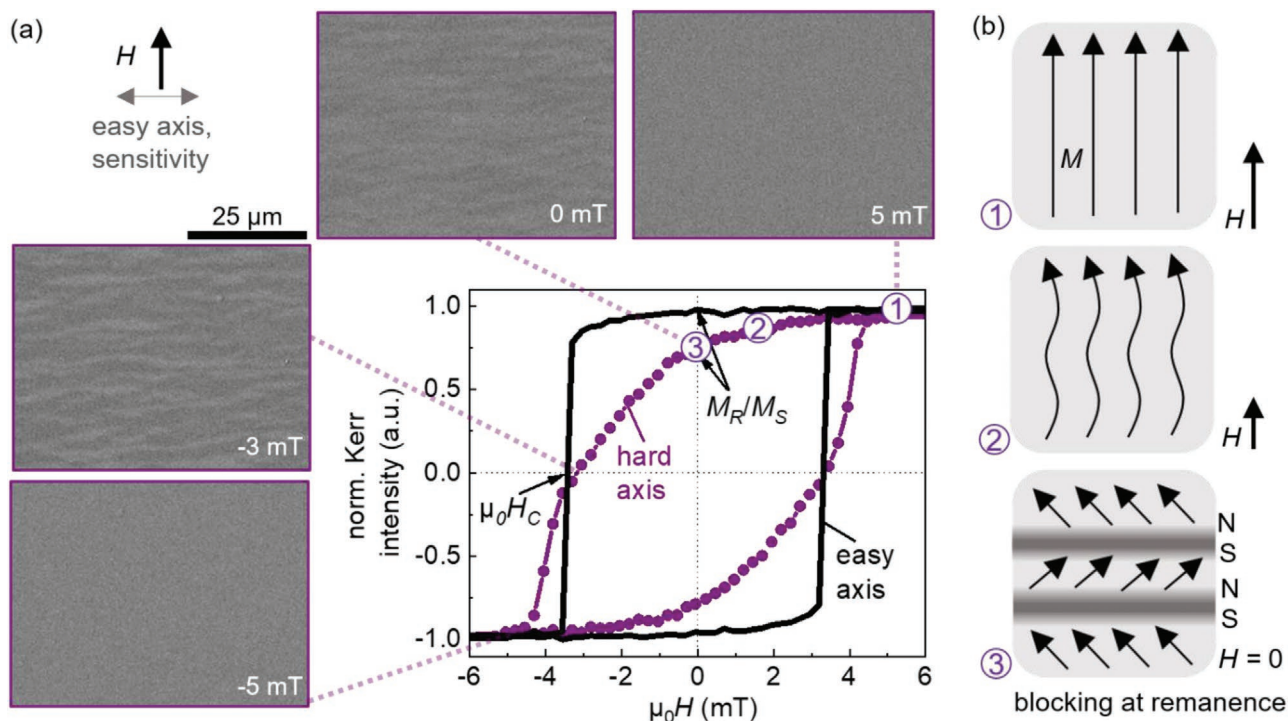


Figure 2. Blocked magnetic domain state in pristine FeO_x/Fe thin films a) In-plane magnetization curves along the easy axis and the hard axis as measured by Kerr magnetometry. For the hard axis magnetization, associated Kerr microscopy images with the Kerr sensitivity along the easy axis (orthogonal to the hard axis) are added. The numbers refer to those in panel (b). b) Schematic of the development of the blocked state in a magnetic field along the (in-plane) hard axis. Starting from the saturated state (①), a fluctuating magnetization (②) forms that leads to the development of the blocked magnetic state (③) with high M_R/M_S ratio. The magnetic charges of the Néel walls are marked by magnetic poles (N – North pole, S – South pole).

fluctuations of magnetization (⊙) develop out of an incipient ripple structure.^[55] Such magnetic fluctuations are caused by statistical perturbations from the random distribution of crystal anisotropy in polycrystalline films, inhomogeneous strain, texture, or non-magnetic impurities.^[56] On decreasing the magnetic field further, the amplitude of the fluctuation of the magnetization becomes larger and, eventually, the magnetization splits in narrowly spaced magnetic domains separated by domain walls.^[51,53,57] The Kerr microscopy images in Figure 2a confirm the evolution of very narrowly spaced magnetic domains elongated along the easy axis. In the present iron films, Néel walls form because the iron-layer thickness is well below the Bloch-Néel transition thickness of ≈ 40 nm (see Figure S5 in the Supporting Information). Further rotation of magnetization upon decreasing the magnetic field is then impeded by the increasing interaction of the magnetic stray fields of the neighboring magnetically charged Néel walls. The stray field of one wall acts as an effective magnetic field for the adjacent wall, finally leading to a blocked magnetic domain state (⊙) and consequently to $M_R/M_S \neq 0$ at zero field.^[52] In a field of opposite polarity (not shown in Figure 2b), the blocking breaks down by the nucleation and motion of Bloch lines.^[51] The pinning of Bloch lines can give rise to large hysteresis and coercivity, especially in very thin films where Bloch lines are easily caught by non-magnetic voids in the films.^[51] In the FeO_x/Fe films from the present study, the grain-boundary oxides are considered to be active pinning sites that explain the large coercivity. The comparison with $\text{Au}/\text{Fe}/\text{Au}$ layers (see Figure S4, Supporting Information), where Au, instead of FeO_x , fills the dents between the iron grains, shows that the magnetic nature of the oxide layer is not relevant for the blocking mechanism. High-resolution Kerr microscopy of the demagnetized state (Figure S5, Supporting Information) did reveal the Néel walls and the existence of Bloch lines. We thus infer that the occurrence of the blocked state and the large hysteresis in the FeO_x/Fe films from the present study are due to interactions of Néel walls with each other and with the microstructural features.

2.2. Reduction/Oxidation Leads to Reversible Voltage-Induced Collapse of Coercivity and Remanence

Until now, the magnetization processes in magnetic thin films are tailored mainly via irreversible changes in microstructure and anisotropy. For example, a change from blocked to “close to ideal” hard-axis behavior is achieved by means of an increased degree of misalignment during epitaxial growth or decreased film roughness.^[54,55,58] In this study, magneto-ionic control of the blocked FeO_x/Fe films was targeted by voltage-induced reversible oxidation and reduction reactions in alkaline electrolyte. The stability of the FeO_x/Fe layer in this electrolyte is an important precondition. In situ RBS (Figure 1b) and in situ magnetometry (Figure S6, Supporting Information) revealed that the nominal iron-layer thickness and the magnetic properties of the FeO_x/Fe films, respectively, remain stable upon immersion in an aqueous LiOH electrolyte.

Reversible electrochemical reduction/oxidation reactions in the FeO_x/Fe layer are expected when specific external voltages^[59] are applied via the electrolyte. In situ Raman measurements (Figure 3a) confirmed a voltage-induced phase transformation in the FeO_x/Fe films. In the pristine state, the characteristic peak at 665 cm^{-1} identifies Fe_3O_4 in the native iron-oxide layer. After adding the electrolyte, a Raman measurement was first carried out in the open circuit potential (ocp) state, i.e., the state of the FeO_x/Fe layer in the electrolyte without additional external voltage applied. In this ocp state, the Fe_3O_4 peak can still be clearly observed despite the increased electrolyte-induced background level in the in situ Raman measurement. When a reduction potential of -1.10 V is applied, the Fe_3O_4 peak vanishes, evidencing a voltage-induced iron oxide-to-metal transformation. The complete disappearance of the Raman signature of Fe_3O_4 indicates that a full transformation of Fe_3O_4 to iron metal occurs. This is in line with the evaluation of the transferred charge during the reduction (see Figure S7, Supporting Information). The Fe_3O_4 peak reappears after

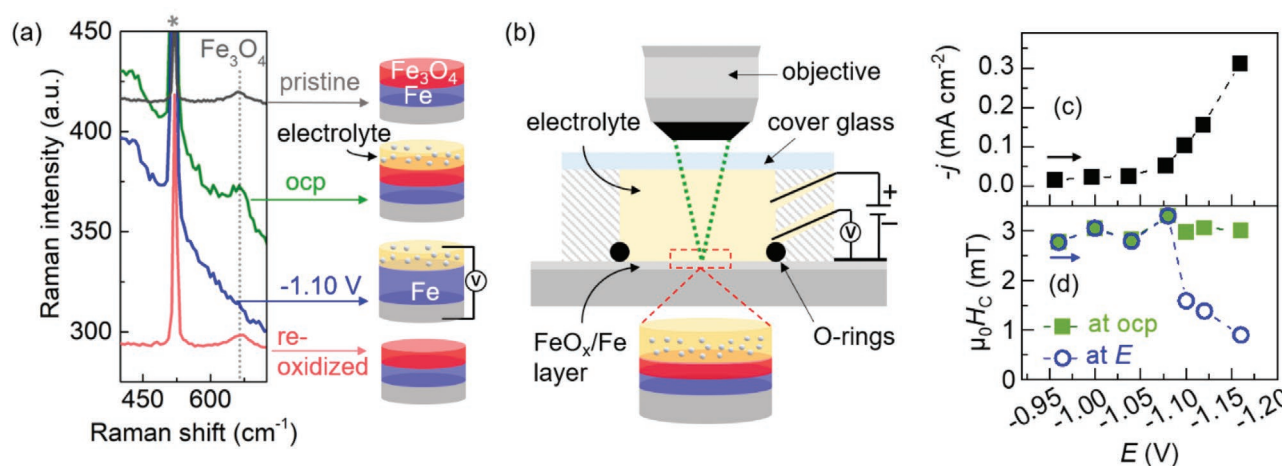


Figure 3. Voltage-control of the coercivity by electrochemical reduction of iron oxide. a) Raman spectra for the same $\text{FeO}_x/\text{Fe}/\text{Au}$ layer in the pristine state, in the electrolyte at the ocp state, in the electrolyte at a reduction potential $E = -1.10\text{ V}$, and after reoxidation and electrolyte removal. The asterisk indicates the substrate peak. The native Fe_3O_4 peak vanishes during the reduction (oxide to metal transformation at -1.10 V) and reappears during reoxidation (metal-to-oxide transformation). Schemes for the different states are displayed on the right. b) Sketch of the electrochemical cell combined with a wide-field Kerr microscope. c,d) Reduction current density $-j$ – c) and simultaneously measured coercivity along the in-plane easy axis d) in dependence of the applied potential. The coercivity of the samples at the ocp state, measured prior to the voltage-gating, is included in (d).

reoxidation of the reduced metal state, which establishes the reversibility of the reduction reaction.

To characterize the voltage-dependency of the reduction reaction, and to reveal associated magneto-ionic changes, the current density and the magnetic properties of the FeO_x/Fe films were measured simultaneously at selected cathodic potentials E . For each voltage step, E was applied for 60 s and a new pristine sample was used in each case to exclude the effects of previous treatments. The magnetization curve measurement was performed through the electrolyte by MOKE magnetometry in a dedicated in-situ Kerr microscopy setup (Figure 3b). The implemented electrochemical cell was constructed as a three-electrode arrangement with the FeO_x/Fe films as the working electrode. Figure 3c,d shows the observed E -dependency of j and H_C , respectively, along the in-plane easy axis. No significant changes in current density and coercivity are observed up to $E = -1.08$ V. The strong increase of the cathodic (negative) current density below -1.08 V indicates the onset of the reduction of the iron oxide to metallic iron. Simultaneously, a drastic decrease in coercivity is measured. At -1.10 V the coercivity decreases to 1.6 mT, corresponding to 53% of the initial value at the ocp state. For more negative potentials, a further decrease in coercivity down to 30% is reached but, at the same time, the H_2 evolution reaction becomes a dominant side reaction and hinders the stable operation of the cell.

The simultaneous change of current density and coercivity below the threshold potential of the iron-oxide-to-iron-reduction

reaction confirms that the voltage-induced change in coercivity originates from this electrochemical transformation. By contrast, changes caused by capacitive charging mechanisms should scale linearly with the potential and would not require a threshold potential. The drastic change of coercivity is a first sign of the significant voltage-tunable magnetism that is possible in the present system.

We measured the impact of the reduction at $E = -1.10$ V and reoxidation at $E = -0.02$ V on the magnetic properties along different in-plane magnetic field angles with respect to the pristine state (Figure 4). For all three axes — hard (0°), easy (90°), and intermediate (45°)—the application of the reduction potential leads to a strong decrease in coercivity (Figure 4a–c). Close to the hard axis, both coercivity and remanence almost vanish. Upon reoxidation, the hysteresis loops nearly recover to those of the pristine state for all three directions. The reversibility of this process for 10 cycles is shown as a representative of the coercivity change along the intermediate axis in Figure 4d (top). The associated change in Kerr intensity difference ΔI (Figure 4d (bottom)) reversibly increases and decreases by about 15–20% upon reduction and reoxidation, respectively. For a rough estimate, an increase of 11% in overall M_S is expected for the full reduction of a Fe_3O_4 (3 nm)/Fe (5 nm) bilayer to a single Fe (7 nm) layer. The observed change in ΔI is qualitatively consistent with this, and also with previously observed changes in M_S for FeO_x/Fe films polarized in alkaline electrolytes.^[16]

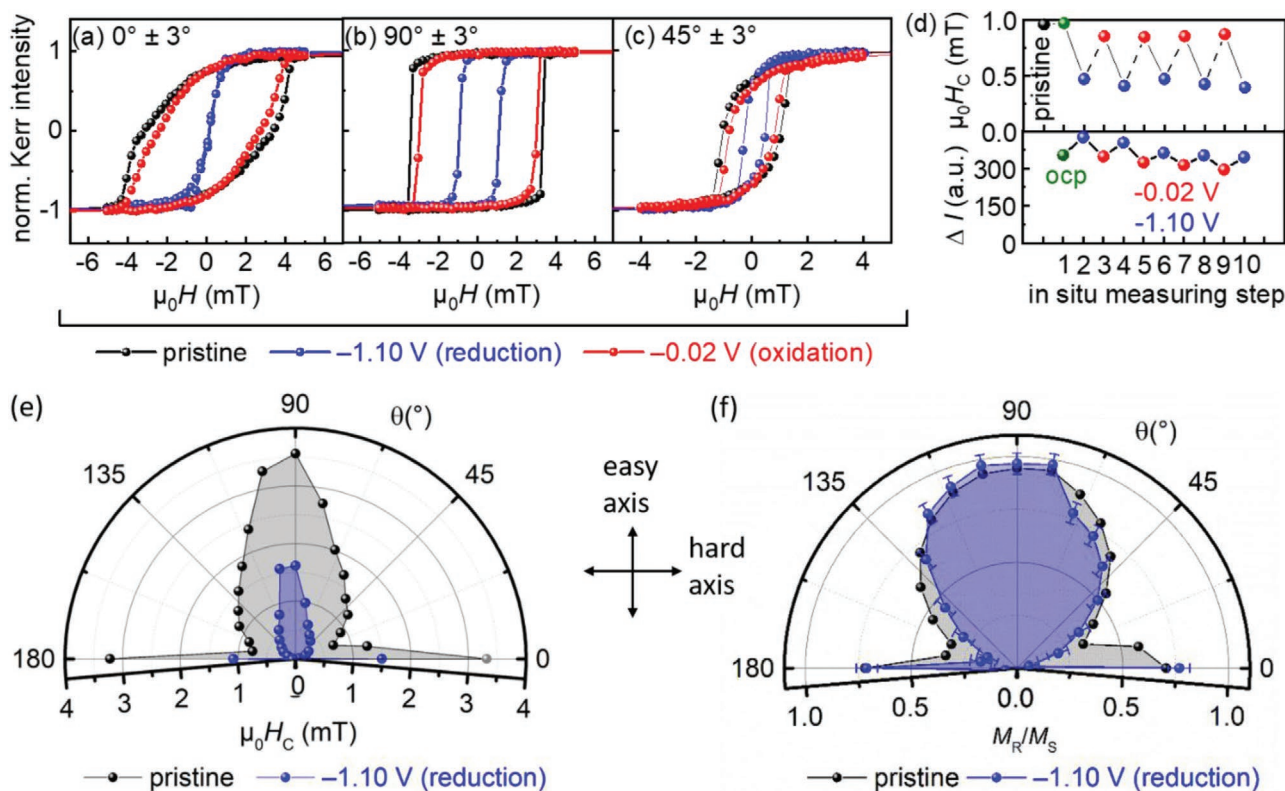


Figure 4. Reversible angle-dependent voltage control of magnetic hysteresis up to ON/OFF switching of coercivity and remanence (magnetic de-blocking). a–c) Magnetization curves of FeO_x/Fe films in the pristine state at -1.10 V (reduction) and -0.02 V (oxidation) measured by Kerr magnetometry with an in-plane magnetic field close to a) the hard axis ($0^\circ \pm 3^\circ$), b) the easy axis ($90^\circ \pm 3^\circ$), and c) an intermediate axis ($45^\circ \pm 3^\circ$). d) Reversible change of coercivity (top) and Kerr intensity difference $\Delta I = I(+5 \text{ mT}) - I(-5 \text{ mT})$ (bottom) along the intermediate axis when repeatedly switching between reduced (-1.10 V) and oxidized (-0.02 V) state. e, f) Angular dependence of e) coercivity and f) M_R/M_S ratio in the pristine state and at -1.10 V (reduced state).

The in plane angular distribution of coercivity and M_R/M_S ratio, respectively, were extracted from angle-resolved Kerr measurements from 0° to 180° in steps of 10° for both pristine (black symbols and gray area) and reduced state (blue symbols and blue area) (Figure 4e,f). The dominant two-fold symmetry reflects the mentioned uniaxial anisotropy. Consistent with such anisotropy, coercivity and M_R/M_S ratio both decrease when turning the field from the easy axis (90°) toward the hard axis (0° , 180°). In the vicinity of the hard axis, the sudden and strong increase in the M_R/M_S ratio and coercivity in the pristine state is consistent with the proposed formation of the blocked state (see discussion in Section 2.1). This deviation from expected “ideal” hard-axis behavior constitutes a peak of M_R/M_S ratio and coercivity in an angle range of $\approx \pm 10^\circ$ around the hard axis (Figure 3e,f).

Remarkably, the voltage-induced reduction leads to a strong decrease in coercivity for all field directions (Figure 4e). In an extended angle range around the easy axis (50° – 130°), coercivity drops to 30–50% of the initial value. The strongest voltage-induced effect on coercivity occurs in the vicinity of the hard axis. Additional measurements with a higher angular resolution close to the hard axis confirm a drastic voltage-induced decrease in coercivity to 5% of the initial value (Figure S8a, Supporting Information). For the M_R/M_S values (Figure 4f), changes upon voltage-induced reduction are negligible for angles close to the easy axis, whereas a significant decrease in M_R/M_S to 10% of the initial value (Figure S8b, Supporting Information) is measured when approaching the hard axis. To summarize, the strongest voltage-induced coercivity and M_R/M_S ratio changes are achieved when magnetic fields are applied close to the hard axis, where a blocked magnetic state is initially present.

The comparative study of $\text{FeO}_x/\text{Fe}/\text{Au}$ and $\text{Au}/\text{Fe}/\text{Au}$ layers (see Figure S4, Supporting Information) rules out the possibility

that the change in magnetic behavior originates solely from the voltage-induced increase of the iron layer thickness^[14,16,60] or from the removal of a specific iron oxide. Instead, the massive change in the close-to-the-hard-axis behavior indicates that the factors that are key to the evolution of coercivity and the blocked state, namely anisotropy and magnetic microstructure, are modified during the reduction process.

2.3. Anisotropy Shows That Anisotropy Varies Inversely with Coercivity Upon Voltage Application

Anisotropy is a key factor for the evolution of coercivity. Therefore, we studied the anisotropy and the anisotropy fluctuations in both pristine and reduced states in greater detail. The similar shapes of the angular H_C - and M_R/M_S ratio distributions for the pristine- and reduced states in Figure 4e,f confirm that uniaxial anisotropy continues to predominate. However, larger relative angle-dependent M_R/M_S and H_C changes are observed in a normalized plot (Figure S8c,d, Supporting Information), which indicates that the magnitude of the uniaxial anisotropy increases in the reduced state.

The uniaxial anisotropy constant, in case of a vanishing remanence and coercivity, can be determined directly from the magnetization curve along the hard axis, if it reveals a linear behavior up to saturation. This is not possible for our iron films owing to the large hysteresis along the hard axis (Figures 2a and 4a). To obtain magnetization curves without hysteresis, the curves along the hard axis were measured in the anhysteretic mode (experimental details see Section 4).

The anhysteretic magnetization curves (Figure 5) consist of a linear part at lower magnetic fields and a partly

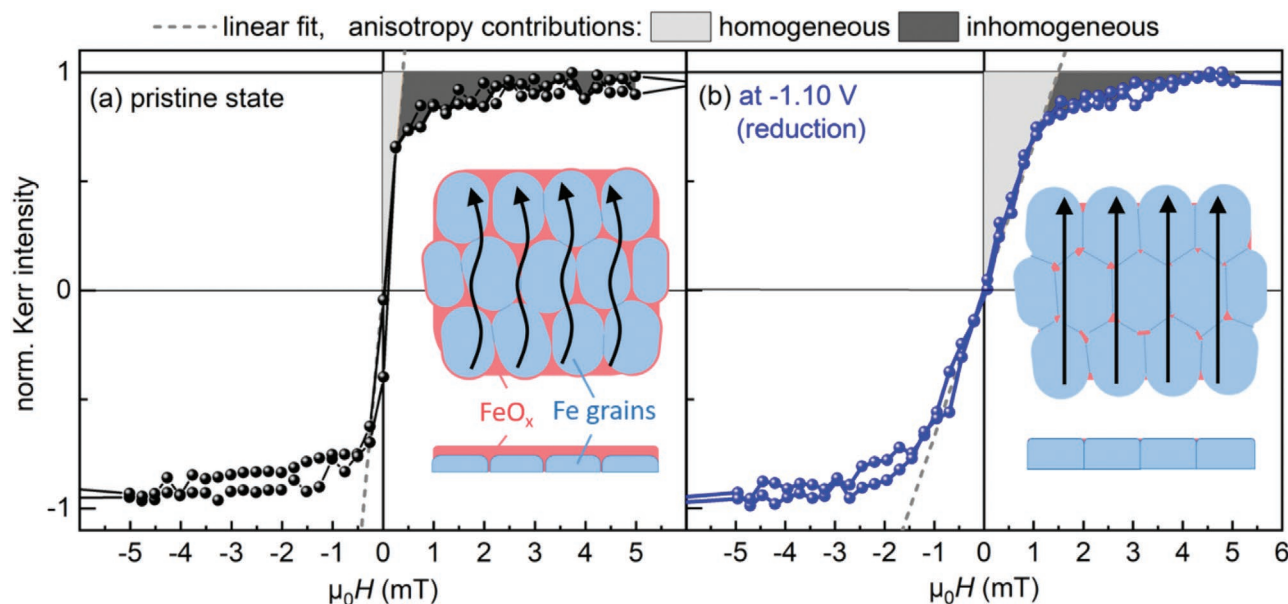


Figure 5. Determination of voltage-induced anisotropy change. a,b) Anhysteretic magnetization curves of FeO_x/Fe films as measured by Kerr magnetometry along the in-plane hard axis for a) the pristine state and b) at -1.10 V (reduced state). Separation of homogeneous and inhomogeneous anisotropy contributions by a linear fit in the low magnetic field region. The sketches in both panels illustrate the proposed microstructural origin. In the natively oxidized state (a), strong anisotropy fluctuations can result from an inhomogeneous microstructure and grain boundary iron oxides, which partially decouple the individual iron grains and yield local variations of the easy axis. In (b) the decrease of the anisotropy fluctuations can be explained by the reduction of the grain boundary oxides into iron, which homogenizes the microstructure and allows better coupling between the iron grains.

nonlinear contribution at higher magnetic fields until saturation; the two parts identify homogenous and inhomogeneous anisotropy contributions, respectively.^[61] Clearly, homogeneous anisotropy increases strongly upon reduction. The anisotropy field, obtained by extrapolating the linear part of the anhysteretic magnetization curve to saturation, changes from 0.4 mT in the pristine state to 1.4 mT in the reduced state. The associated uniaxial anisotropy constants (K_u) of 326 and 1202 J m⁻³ for the pristine and reduced state, respectively, are estimated from the respective areas of the homogeneous anisotropy contribution depicted in Figure 5 by assuming the saturation magnetization of (bulk) iron, $M_{S,Fe} = 1710$ kA m⁻¹. The complex evolution of the anisotropy in nanocrystalline two-phase systems currently prevents us from unambiguously determining why the anisotropy increases upon reduction. We speculate that the increase could be attributed to an anisotropic change in the grain shapes/sizes or roughness of iron upon electrochemical iron-oxide reduction. In addition, an electronic-charge-induced modulation of the interface PMA of the iron layer,^[62] caused by superposed electrochemical double-layer formation at the reduction potential, may play a minor role. An increase of in-plane uniaxial anisotropy resulting from a voltage-induced decrease of interface PMA has been reported for vicinal iron films, even considerably thick ones (35 monolayer).^[63] However, at this thickness, the effects are significantly smaller than those observed in the present films.

Figure 5 also shows that reduction leads to a strong decrease of the inhomogeneous anisotropy contribution and, thereby, of the anisotropy fluctuations. We infer these changes to result from the microstructural modifications expected during the electrochemical process. In the pristine state (Figure 5a), the exchange coupling between the iron grains is affected by the native oxide at the grain boundaries. The grain boundary oxide does not completely suppress the exchange coupling between the grains (a highly coercive, particulate media would be the consequence), but rather leads to a reduction of the effective exchange coupling. According to the random anisotropy model,^[64] the exchange interaction can average out the magnetocrystalline anisotropy of the iron grains. A decreased exchange coupling thus leads to stronger fluctuations of the effective uniaxial anisotropy axis—that is, increasing inhomogeneous anisotropy. The application of -1.10 V leads to the reduction of the native oxide, starting at the FeO_x/Fe interface.^[60] As a consequence, the grain boundary oxides are reduced to metallic iron, which is expected to yield a better exchange coupling between the iron grains and thus a homogenization of the anisotropy and magnetic microstructure (compare the sketches in Figure 5a,b). This can explain the observed decrease in the inhomogeneous anisotropy contributions.

The increase of homogeneous anisotropy occurring simultaneously with the drastic decrease in coercivity upon reduction shows that the direct proportionality between anisotropy and coercivity, which is often used as a simple model for magnetoionic and magnetoelectric effects,^[6,65,12] is not applicable here. Instead, it is likely that changes in microstructure or magnetic domain structure dominate over direct anisotropy effects, as discussed in the next section.

2.4. In Situ Kerr Microscopy Reveals Voltage-Induced Domain Structure Changes

The magnetic domain observations were made with an in situ Kerr microscopy setup, which resolves the magnetic domains concurrently with electrochemical polarization in the liquid electrolyte. Figure 6 shows the AC-demagnetized states, which resemble domain states close to zero-field equilibrium, for a pristine FeO_x/Fe film and for the same film in the electrolyte at the ocp, reduction (-1.10 V), and oxidation (-0.02 V) states. For all images, the demagnetizing is carried out along the hard axis and the Kerr sensitivity is set along the easy axis. The domains are observed to extend along the easy axis and their somewhat irregular shape is typical for polycrystalline thin films with uniaxial anisotropy and Néel walls.^[51] The average magnetization in the domains is aligned along the easy axis (marked exemplarily with the black and white arrows in Figure 6a). As expected, the magnetic domain character and width are not altered by the electrolyte contact (pristine vs ocp state). While applying the reduction voltage of -1.10 V, the shape of the domains remains comparable but a strong increase in domain width is observed. During reoxidation (-0.02 V), the average domain size decreases again and the domain image resembles that of the pristine and ocp states. For the pristine-, ocp-, and reoxidized states, all of which are characterized by the presence of an iron-oxide cover layer, the average domain width is ≈ 6 μ m (Figure 6e). By contrast, the average domain width in the reduced state is ≈ 14 μ m. An example for the domain width analysis is given in Figure S9 (Supporting Information).

The observations described above point clearly to a significant voltage-induced change of the equilibrium magnetic domain width upon oxidation/reduction. This increase of domain size could be caused by an increase in domain-wall energy, which results in an energy-saving decrease in the number of domain walls. We calculate the change in the domain-wall energy upon reduction by accounting for an increase in iron-layer thickness from 5 to 7 nm, which is expected during the reduction process,^[14,60] and by considering the measured changes in K_u (see Section 2.3 and S10, Supporting Information.). This calculation shows that an increase in domain-wall energy of 40% can be expected during the reduction process, which could explain the decrease in the number of domain walls and the associated increase in the equilibrium domain size.

2.5. Voltage-Induced Magnetic Deblocking Relates to Change of Néel Wall Interactions

Based on the results presented above, we propose a consistent mechanism that connects the voltage-induced changes in hysteresis, anisotropy, and domain size with the reduction/oxidation process. Since the magnetization processes are distinctly different for fields along the hard and easy axis, both are addressed individually.

For the hard-axis case, the impact of oxidation and reduction on the hysteresis can be explained by the interplay of the anisotropy change and the specific properties of the magnetically charged Néel walls. The blocked state, which causes the large coercivity and remanence along the hard axis in the pristine

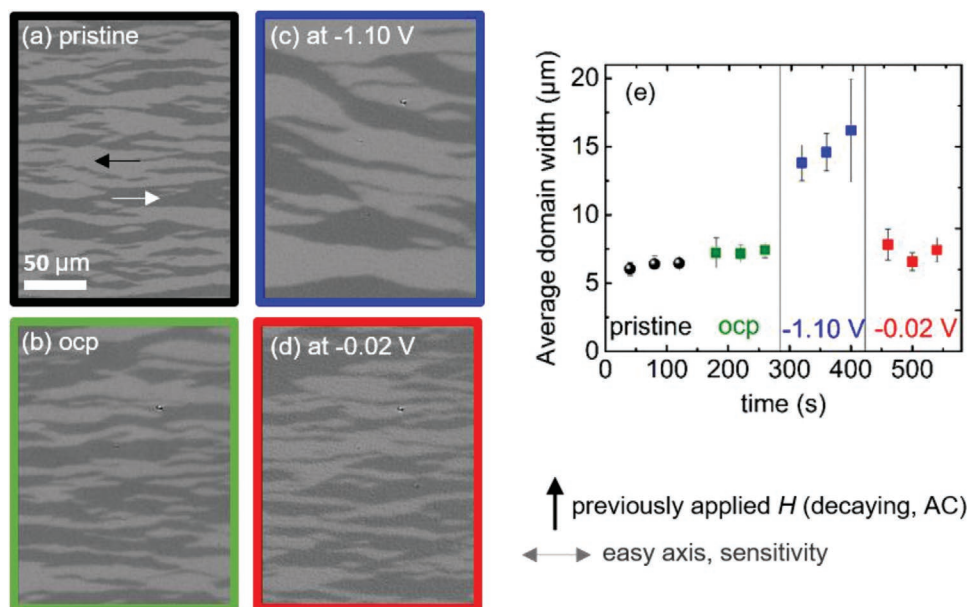


Figure 6. Voltage control of the magnetic domains. a–d) Magnetic domains observed by in situ Kerr microscopy a) in the pristine state, b) in the ocp state, c) at -1.10 V (reduction), and d) at -0.02 V (oxidation). The images were acquired after a decaying 20 Hz AC field was applied perpendicularly to the easy axis. e) Average domain size, extracted from the domain images for the four states (a–d). For each state, the AC routine and domain image acquisition was repeated three times.

(oxidized) state (Figure 2), originates from the interaction between the extended tails of the Néel walls. The tail width w_{tail} depends strongly on the anisotropy,^[51] which implies that the voltage-induced change in K_u also changes w_{tail} . For symmetric Néel walls, w_{tail} is determined by a balance between the magnetic charge distribution, described by the maximum stray field energy density (K_d) and the anisotropy energy (K_u):^[51]

$$w_{\text{tail}} = e^{-\gamma} dK_d/K_u \approx 0.56 dK_d/K_u \quad (1)$$

where $\gamma = 0.577$ is the Euler-Mascheroni constant and d is the film thickness. For the present case, we use the K_u values obtained from the anhysteretic measurements and iron-film thicknesses of 5 and 7 nm for the pristine (oxidized) and reduced state, respectively, in Equation (1). With those values, we obtain tail widths of 24.1 and 8.4 μm for the pristine (oxidized) and reduced state, respectively. This indicates that w_{tail} decreases concurrently with the increase in domain size upon reduction. For parallel walls, wall interactions play a role as soon as an overlap of the Néel wall tails occurs, i.e., when the domain width $< 2 w_{\text{tail}}$.^[51] For the oxidized state, strong interaction is expected as the average domain width of around 6 μm is much smaller than $2 w_{\text{tail}} = 48 \mu\text{m}$. This is consistent with the emergence of a strong blocking. Upon reduction, the values for the average domain size of 15 μm and $2 w_{\text{tail}} = 16 \mu\text{m}$ are similar. Even though this comparison is carried out on the basis of equilibrium domains, a qualitatively similar trend is expected and observed (Figure S11, Supporting Information) for the domains present in the remanent state. We expect that significantly fewer interactions between the walls will occur in the reduced state, which is consistent with the observed deblocking. We can thus conclude that the voltage-induced switching from a blocked state to a “close-to-ideal” hard-axis

behavior with negligible remanence and coercivity, and vice versa, results from a change in amplitude of the Néel wall interactions. This change in wall interactions, in turn, originates from anisotropy-related decrease/increase in Néel wall tail width in combination with the coarsening/refinement of the magnetic microstructure.

If the field is applied along the easy axis, the decreased coercivity (see Figure 4a–e) upon reduction, concurrent with an increased anisotropy, seems unexpected at first glance. However, this need not be the case if we bear in mind that coercivity is an extrinsic property and depends on both, anisotropy and microstructure. In this study, the voltage-induced K_u and coercivity vary inversely, which implies that microstructural effects dominate over the anisotropy effects. We propose that this is due to the electrochemical modification of the grain boundary oxides, which can act as pinning centers for the magnetic domain walls in the pristine state. Upon reduction, the defective iron oxide centers will transform to ferromagnetic iron and thereby lose the pinning functionality. In addition, the homogenization of the ferromagnetic iron surface and better exchange coupling of the individual iron grains are expected, which is in agreement with the measured increased homogeneity of anisotropy in this study. All three effects can contribute to the drastic decrease in coercivity along the easy (and also intermediate) axis. Until now, similar effects have been well known for magnetic materials in which grain boundaries are altered in an irreversible way. For example, a decrease of coercivity is observed when switching from decoupled nanogranular structures to coalesced FePt films.^[66] Also, for $\text{Nd}_2\text{Fe}_{14}\text{B}$ magnets, the control of coercivity and remanence relies on the tuning of the exchange coupling between the $\text{Nd}_2\text{Fe}_{14}\text{B}$ grains, which is achieved by the optimization of the nature and distribution of intergranular phases.^[67] The present study demonstrates that

similar coercivity control can be achieved in a reversible way by voltage-induced iron-oxide reduction and reoxidation in thin films. The magnetic changes in our FeO_x/Fe thin-film system are reversed within seconds (see following section) and are also fully reversible during several voltage switching steps.

2.6. Switching of Magnetization by a Low Voltage

Magnetization switching by 180° , induced by an electrical field instead of magnetic fields, is of general interest in magnetic devices and is desired for such applications as logical operation modes. The reversible collapse of coercivity by voltage-triggered reduction that we document from the present study offers a direct route to voltage-induced switching of magnetization by 180° in the presence of a small magnetic bias field. This is demonstrated in Figure 7 as compared with conventional magnetic-field switching along the magnetic easy axis.

The starting point is the ocp (oxidized) state, which is saturated at $H = +20$ mT and which exhibits a coercivity of 3.7 mT. Conventional M -switching under magnetic field control (green curve in Figure 7a) was probed via in situ Kerr microscopy (see the Figure S12 and the video, Supporting Information). The magnetization reversal can be followed from the Kerr micrographs, starting with the saturated state (upper image in Figure 6b), followed by the switching via nucleation and growth of reverse domains (middle image) and ending with the fully switched state with reverse magnetization (bottom image). To demonstrate E -induced switching, the same sample, again after saturation in $H = +20$ mT, is held at $H = -2$ mT. In this state, the magnetization is still fully aligned in the direction of the previously applied positive magnetic field. The application of $E = -1.10$ V leads to a reduction of coercivity and consequently to magnetization reversal, which can be followed by the domain images in Figure 7c. The voltage is applied after 10 s at a magnetic field of -2 mT. At this time, the fully saturated state is probed (upper image in Figure 7c). After about 30 s at -1.10 V, reverse domains nucleate and grow (middle image). Full switching occurs within 2 s (bottom image). This M -switching is unambiguously caused by the voltage application: a control experiment for the same sample at -2 mT at ocp showed that no change in magnetic state occurs within 120 seconds without applied voltage (see Figure S12 and video, Supporting Information). After the voltage-induced M -switching, a hysteresis with significantly lower coercivity, as expected for the reduced state, is measured (blue curve in Figure 7a).

Remarkably, the E - and H -controlled magnetic reversal proceed in a similar manner. This becomes evident from the comparison between the domain images during the switching processes (Figure 6b,c), which show similar locations and shapes of the growing reverse domains. This indicates that the nucleation sites and the local distribution of pinning sites that affect the reverse domain growth do not change substantially during the reduction process. However, the E -induced switching proceeds at much lower (constant) H , which points to a substantially reduced pinning strength. These observations are consistent with the electrochemical effect on the grain boundaries as pinning sites. The local distribution of the grain boundaries remains similar upon reduction/oxidation

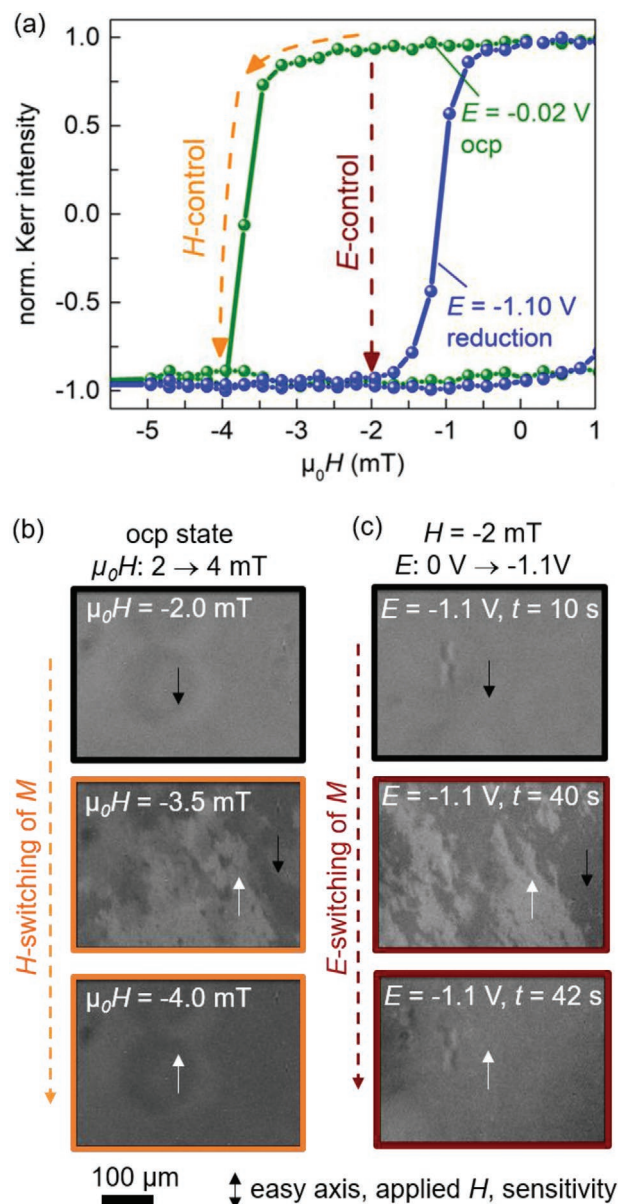


Figure 7. E -induced 180° switching of magnetization by a low voltage. a) Pathway for E -induced magnetization reversal based on the voltage-induced change from a high H_C -state (ocp state, green curve) to a low H_C -state (-1.10 V, reduced state, blue curve) at a small bias field of -2 mT. The conventional magnetic field-controlled magnetization reversal is indicated for comparison. Domain evolution at the same sample position during b) the H -induced and c) the E -induced magnetization reversal. These in situ Kerr images were extracted from a video camera monitoring the switching processes (see S12, Supporting Information). The sample was saturated at $+20$ mT prior to switching in both cases.

processes, since the boundaries between the randomly oriented grains do not disappear. Their pinning strength, however, decreases strongly from the oxidized (weakly magnetic) to the nonoxidized (magnetic) state during the voltage-triggered reduction process (as discussed in Section 2.5).

The voltage-induced change of equilibrium domain size indicates that at a local scale, the voltage-induced switching

of magnetization should proceed even without an additional external magnetic field. Currently, this effect cannot be resolved because of the very fine magnetic microstructure at remanence, in conjunction with the limited resolution of our in-situ Kerr microscope set up (which relies on objective lenses with long working distance, i.e., limited resolution and magnification). However, the effect may be observable by in-situ magnetic force microscopy. The voltage-induced displacement of the domain walls, either by modified domain-wall interactions or a change of the pinning strength, could be of interest for domain-wall logic concepts.^[68] In comparison to domain size modulations achieved by capacitive electronic charging in a sub-nanometer Co layer when applying ± 10 V,^[69] the present ionic mechanism for domain size control requires a much lower voltage (1 V) and opens the door to a nonvolatile setting of the local magnetization.

2.7. Energy Efficiency and Application Potential for Data Storage and Actuation

In the magneto-ionic approach presented here, voltage-induced changes in phase and microstructure allow the reversible tuning of technologically important magnetic properties at room temperature. For example, during the process of writing in magnetic storage devices, the state with low coercivity and associated easy magnetization switching, could be set by voltage. As compared with heat-assisted magnetic recording, where the decrease in coercivity and switching of magnetization are controlled by laser heating, the control of coercivity by voltage is a more energy-efficient approach. In addition, the setup is possibly simpler, even though addressing a single bit by an electric field remains an engineering challenge. We evaluate the switching energy required for changing coercivity, remanence, and the direction of magnetization from the time integral of the measured electric current multiplied by the applied voltage. An energy of 121 mJ is calculated for switching the large area (38.5 mm²) and for conservatively assuming a switching time of 60 s. To facilitate comparison with current memory devices, the energy per typical bit area was evaluated within a simple model assuming a linear dependency between switching energy and device area. For a circular area with a diameter of 50 nm (3 nm), typical for high density longitudinal (perpendicular) magnetic recording media, this calculation yields a switching energy of 618 fJ (5 fJ). These energy values approach the order of magnitude of the lowest reported switching energies, namely 6 fJ for a magnetic tunnel junction device with 50 nm diameter, switched in a much shorter time of 0.5 ns.^[70,71] Previous studies on memristive systems have shown that redox-based mechanisms^[71] can also yield switching times down to the sub-ns regime. This indicates that the presented magneto-ionic mechanism can yield an improvement in the energy efficiency of several orders of magnitude.

The ionic mechanism could be applied imminently to magnetic films with higher and/or perpendicular magnetic anisotropy to achieve stable magnetization at small bit size. For example, for a granular high density FePt media, a redox-tunable iron oxide/iron overlayer^[16] could be exploited in a similar manner to achieve voltage-induced decoupling and coupling of the FePt grains and, thus, tunable coercivity. As an alternative,

higher anisotropy and stability of magnetization may be possible via the exchange-bias effect achieved in combination with an antiferromagnetic underlayer.

The demonstrated energy-efficient switching of coercivity and remanence, both of which are key parameters for the energy product of magnetic materials, could also be applied in micro- and nanoactuation. At present, integrated electromagnets offer flexibility in field strength as well as easy ON/OFF switching at the microscale, but they require sophisticated coil design, are limited in field strength, and cause undesired Joule losses.^[72] Further, the energy consumption of microelectromagnets increases strongly with decreasing dimension, which impedes their use at the nanoscale.^[73] Our study points to a fundamentally new route toward tunable nanomagnets with voltage-programmable energy product and associated magnetic stray fields, and thus toward a low power alternative to microelectromagnets.

The ionic mechanism presented here works for films covered by native oxide layer and thus does not require specific preparation or surface treatment. This robustness presents a key advantage over other magnetoelectric tuning mechanisms. Moreover, large reversible effects are obtained in ferromagnetic metal films beyond the ultrathin limit in ambient conditions and at room temperature, a combination that is not yet possible with conventional magnetoelectric approaches.

3. Conclusion

We demonstrate a fully reversible low-voltage-induced collapse of coercivity and remanence in FeO_x/Fe thin films at room temperature, accompanied by large anisotropy and domain structure changes. The magnetic changes are induced by the reversible reduction and reoxidation of the iron-oxide layer. Detailed analysis of the impact of this phase change on the magnetic hysteresis and domains indicates a magneto-ionic deblocking mechanism, connected to changes in the microstructure and the structure of magnetic domains.

In the initial (oxidized) state, a blocked state that exhibits a large hysteresis for the hard axis direction is stabilized by Néel wall interactions. Upon reduction of the iron oxide, the increase in anisotropy and iron-layer thickness can lead to a larger domain wall energy, and thereby cause the observed increase in domain size. As a result of the coarsening of the magnetic microstructure and the decrease of the Néel wall tail width, the domain-wall interactions are weakened, and the magnetically blocked state is suppressed. This is followed directly by the voltage-induced switching from a large hysteresis along the hard axis to “close to ideal” hard-axis behavior. The decreased pinning strength of the grain boundaries upon iron-oxide reduction can cause the collapse of the coercivity along all other directions.

The apparent contradiction that a decreased coercivity is obtained at increased anisotropy can be resolved by accounting for the role of the microstructure and the magnetic domains. Coercivity and anisotropy thus do not need to necessarily scale with each other, an important consideration for magneto-ionic materials involving changes in phase and microstructure. This consideration opens a route

beyond the state-of-the-art thin-film magneto-ionics, in which extrinsic properties such as coercivity are usually changed by controlling the intrinsic perpendicular magnetic anisotropy. The voltage-induced modification of local defects presents a paradigm change in ionic control of magnetism, which so far commonly affect the interface or the bulk of the material as a whole. For the local control of defects only a small portion of the material needs to be affected. This promises a higher energy efficiency and faster speed than conventional magneto-electric approaches. The magneto-ionic mechanism presented in this paper fulfills the important requirements of room temperature and ultralow power operation of future magnetic devices, especially in the fields of magnetic memory, domain wall logic, neuromorphic computing, and magnetic actuation devices. The mechanism of voltage-controlled defects may be transferrable to many other defect-controlled materials, such as type II superconductors or materials with specific mechanical properties.

4. Experimental Section

Preparation of the FeO_x/Fe Thin Films: The Fe/Au/Cr layered architecture was prepared by DC magnetron sputtering with a base pressure of 2×10^{-8} mbar at room temperature. Thermally oxidized Si(100) wafers were used as the substrate. During the gold and iron deposition, the substrate was rotated at 0.67 rpm and the target guns were inclined at an angle of 45° with respect to the substrate normal. Argon with 2% hydrogen was used as sputtering gas. After removal from the vacuum chamber, the exposure of the Fe/Au films to ambient condition led to the formation of an iron-oxide surface layer.

Characterization of Iron Layer Thickness and Stability in the Electrolyte: In situ Rutherford backscattering measurements were conducted to investigate the thickness and stability of the layer in contact with the electrolyte. The layered film was deposited on a Si₃N₄ window with a thickness of 500 nm. The different substrate is not expected to affect the film properties as both Si₃N₄ and SiO are amorphous. The substrate was attached to the beamline instrumentation in such a way that the backside faced vacuum (10^{-6} mbar) and the iron layer faced either air or the electrolyte. The He⁺ ion beam of 1.7 MeV energy was generated by a 2 MV van de Graff accelerator and guided via switching magnets toward the sample. The obtained spectra were evaluated using SIMNRA^[74] software. No difference is made between iron and iron oxide in the evaluation, because the differences in the mass density are not known exactly (but they are expected to be small).

Characterization of Microstructure: High resolution transmission electron microscopy was conducted on a double-aberration-corrected FEI Titan3 80–300 microscope to investigate the architecture and microstructure of the film. The preparation of the cross-section lamella, cut parallel to the easy axis, was carried out via focused ion beam technique on a FEI Helios Nanolab 600i using 30 and 4 kV Ga⁺ ions. Further thinning of the lamella was performed in a Gatan PIPSII with 0.2 kV Ar⁺ ions. The crystallographic orientations of the layers were determined by performing a fast Fourier transform in the Gatan Microscopy Suite of the respective sample areas.

Electrochemical Procedures: A LiOH (1 mol L⁻¹) aqueous solution was used as electrolyte. The FeO_x/Fe thin film samples were connected as the working electrode, while platinum wires served as counter- and reference electrodes. The potentials, *E*, quoted in this work represent the potential of the working electrode in Volt versus the platinum reference electrode. The formula symbol *E* for the electrode potential is chosen according to the IUPAC definition for electrochemistry (it is not equivalent to the electric field). The application of *E* and the measurement of the *j*(*E*) characteristics were performed with a potentiostat (Biologic SP50).

Characterization of Iron Oxide Reduction and Reoxidation via In Situ Raman Spectroscopy: Raman spectra were recorded on a T64000 triple spectrometer (Jobin Yvon) Horiba, equipped with a diffraction grid of 600 g mm⁻¹ and a 532 nm excitation wavelength of a Torus 532 laser (Laser Quantum). The ex situ measurements were carried out with a Leica PL FLUOTAR 50x objective and with the laser power adjusted to less than 7.3 μW (laser spot diameter of 20 μm on the sample).^[75] An UMPlanFLN 20XW Olympus water immersion objective was used for the in-situ measurements. *E* was applied by the potentiostat in a two-electrode configuration.

Electrochemical and Magnetic Characterization in an In Situ Kerr Microscopy Setup: An electrochemical cell built in house, compatible with the Kerr microscopy setup (see Figure 3a and further details in ref. [14]) was used. The electrolyte compartment hosted 200 μL of electrolyte solution, and a circular area of 38.5 mm² of the FeO_x/Fe thin film sample, defined by a sealing ring, was exposed to the electrolyte. The cell was operated in a three-electrode configuration. A cover glass was placed on top of the cell to achieve a planar surface required for in situ Kerr magnetometry and microscopy. An objective lens guided the light through the cover glass and the electrolyte, which was sealed by a surrounding Teflon cell. To account for the different refractive indices of the cover glass and the electrolyte, a long-distance objective (Zeiss LD ACHROPLAN with 40x magnification) with a collar ring was used to focus on the sample surface. The measurements for oxidation and reduction states were started 20 s after the respective voltage was applied.

The magnetic hysteresis and domain characterization were carried out with the Kerr microscope with selective sensitivity to pure in-plane magnetization using the longitudinal Kerr effect.^[76] An external magnetic field was applied in the sample plane along the in-plane sensitivity direction of the Kerr microscope. The recorded hysteresis loops were normalized and corrected for drift and Faraday effects in the objective lens and cover glass. The magnetic field direction was calibrated based on the alignment of the magnetic domain walls along the easy axis, yielding a precision of ±3°. For MOKE magnetometry, the Kerr intensity of a selected sample area was plotted as a function of magnetic field.^[49]

An hysteretic magnetization was measured as prerequisite for the separation of homogeneous and inhomogeneous anisotropy contributions. The setup consisted of a DC magnet field sweep, in which a decaying alternating magnetic field was superimposed at each magnetic field value.^[45,55] The separation of the anisotropy contributions was performed using a linear fit up to $a(a-1/e)$, where *a* is the average intensity value in saturation between 5 and 20 mT and *e* is the Euler number.

The AC-demagnetized state to characterize the equilibrium magnetic domains was set upon the application of an alternating magnetic field of 20 mT at a frequency of 20 Hz, which decayed linearly within 20 s parallel to the hard axis. This procedure constantly oscillates the magnetic moments around the easy axis until the external magnetic field is weak enough for the sample to reach thermodynamic equilibrium, in which the magnetic moments fall in a state of lowest energy. The average domain width for each state is calculated from three domain images captured independently after identical demagnetization routines.

Supporting Information

Supporting Information is available from the Wiley Online Library or from the author.

Acknowledgements

The authors acknowledge funding by the DFG (project LE 2558 2-1) and the excellence program initiative of the IFW Dresden. S.S. gratefully acknowledges financial support by the DFG through the priority program SPP2137: Skyrmionics (project number: 403503416). The authors thank

A. Popov and F. Ziegls for help with the in-situ Raman spectroscopy measurements, T. Walter and A. Pöhl for TEM sample preparation, S. Pofahl for technical assistance with Kerr microscopy, R. Voigtländer and S. Glöge for help with the in situ Kerr microscopy cell construction, and N. Perez for discussions on the growth and magnetism of the FeO_x/Fe thin films (all IFW Dresden).

Open access funding enabled and organized by Projekt DEAL.

Conflict of Interest

The authors declare no conflict of interest.

Keywords

iron films, magnetic domains, magnetoelectrics, magneto-ionic mechanisms, Néel walls

Received: April 20, 2020

Revised: August 31, 2020

Published online:

- [1] C. Song, B. Cui, F. Li, X. Zhou, F. Pan, *Prog. Mater. Sci.* **2017**, *87*, 33.
- [2] A. Molinari, H. Hahn, R. Kruk, *Adv. Mater.* **2019**, *31*, 1806662.
- [3] C. Leighton, *Nat. Mater.* **2019**, *18*, 13.
- [4] C. Navarro-Senent, A. Quintana, E. Menéndez, E. Pellicer, *J. Sort. APL Mater.* **2019**, *7*, 030701.
- [5] M. K. Niranjan, C.-G. Duan, S. S. Jaswal, E. Y. Tsybmal, *Appl. Phys. Lett.* **2010**, *96*, 222504.
- [6] M. Weisheit, S. Fahler, A. Marty, Y. Souche, C. Poinsignon, D. Givord, *Science* **2007**, *315*, 349.
- [7] S. Zhao, L. Wang, Z. Zhou, C. Li, G. Dong, L. Zhang, B. Peng, T. Min, Z. Hu, J. Ma, W. Ren, Z.-G. Ye, W. Chen, P. Yu, C.-W. Nan, M. Liu, *Adv. Mater.* **2018**, *30*, 1801639.
- [8] A. Quintana, J. Zhang, E. Isarain-Chávez, E. Menéndez, R. Cuadrado, R. Robles, M. D. Baró, M. Guerrero, S. Pané, B. J. Nelson, C. M. Müller, P. Ordejón, J. Nogués, E. Pellicer, *J. Sort. Adv. Funct. Mater.* **2017**, *27*, 1701904.
- [9] D. Chiba, M. Kawaguchi, S. Fukami, N. Ishiwata, K. Shimamura, K. Kobayashi, T. Ono, *Nat. Commun.* **2012**, *3*, 888.
- [10] A. D. Lamirand, J.-P. Adam, D. Ravelosona, P. Allongue, F. Maroun, *Appl. Phys. Lett.* **2019**, *115*, 032402.
- [11] K. Leistner, J. Wunderwald, N. Lange, S. Oswald, M. Richter, H. Zhang, L. Schultz, S. Fähler, *Phys. Rev. B* **2013**, *87*, 224411.
- [12] U. Bauer, L. Yao, A. J. Tan, P. Agrawal, S. Emori, H. L. Tuller, S. van Dijken, G. S. D. Beach, *Nat. Mater.* **2015**, *14*, 174.
- [13] D. Yi, Y. Wang, O. M. J. van 't Erve, L. Xu, H. Yuan, M. J. Veit, P. P. Balakrishnan, Y. Choi, A. T. N'Diaye, P. Shafer, E. Arenholz, A. Grutter, H. Xu, P. Yu, B. T. Jonker, Y. Suzuki, *Nat. Commun.* **2020**, *11*, 902.
- [14] J. Zehner, R. Huhnstock, S. Oswald, U. Wolff, I. Soldatov, A. Ehresmann, K. Nielsch, D. Holzinger, K. Leistner, *Adv. Electron. Mater.* **2019**, *5*, 1900296.
- [15] K. Taniguchi, K. Narushima, H. Sagayama, W. Kosaka, N. Shito, H. Miyasaka, *Adv. Funct. Mater.* **2017**, *27*, 1604990.
- [16] K. Duschek, D. Pohl, S. Fähler, K. Nielsch, K. Leistner, *APL Mater.* **2016**, *4*, 032301.
- [17] D. A. Gilbert, A. J. Grutter, E. Arenholz, K. Liu, B. J. Kirby, J. A. Borchers, B. B. Maranville, *Nat. Commun.* **2016**, *7*, 12264.
- [18] R. Mishra, D. Kumar, H. Yang, *Phys. Rev. Appl.* **2019**, *11*, 054065.
- [19] J. Lee, W. D. Lu, *Adv. Mater.* **2018**, *30*, 1702770.
- [20] Z. Luo, Z. Lu, C. Xiong, T. Zhu, W. Wu, Q. Zhang, H. Wu, X. Zhang, X. Zhang, *Adv. Mater.* **2017**, *29*, 1605027.
- [21] A. J. Tan, M. Huang, C. O. Avci, F. Büttner, M. Mann, W. Hu, C. Mazzoli, S. Wilkins, H. L. Tuller, G. S. D. Beach, *Nat. Mater.* **2019**, *18*, 35.
- [22] C. Bi, Y. Liu, T. Newhouse-Ilige, M. Xu, M. Rosales, J. W. Freeland, O. Mryasov, S. Zhang, S. G. E. te Velthuis, W. G. Wang, *Phys. Rev. Lett.* **2014**, *113*, 267202.
- [23] N. Di, J. Kubal, Z. Zeng, J. Greeley, F. Maroun, P. Allongue, *Appl. Phys. Lett.* **2015**, *106*, 122405.
- [24] U. Bauer, S. Emori, G. S. D. Beach, *Nat. Nanotechnol.* **2013**, *8*, 411.
- [25] P. Dhanapal, T. Zhang, B. Wang, H. Yang, H. Xuan, C. Bi, W. Wang, R.-W. Li, *Appl. Phys. Lett.* **2019**, *114*, 232401.
- [26] L. Herrera Diez, Y. T. Liu, D. A. Gilbert, M. Belmuguenai, J. Vogel, S. Pizzini, E. Martinez, A. Lamperti, J. B. Mohammedi, A. Laborieux, Y. Roussigné, A. J. Grutter, E. Arenholz, P. Quarterman, B. Maranville, S. Ono, M. S. E. Hadri, R. Tolley, E. E. Fullerton, L. Sanchez-Tejerina, A. Stashkevich, S. M. Chérif, A. D. Kent, D. Querlioz, J. Langer, B. Ocker, D. Ravelosona, *Phys. Rev. Appl.* **2019**, *12*, 034005.
- [27] T. Tsuchiya, K. Terabe, M. Ochi, T. Higuchi, M. Osada, Y. Yamashita, S. Ueda, M. Aono, *ACS Nano* **2016**, *10*, 1655.
- [28] K. Duschek, A. Petr, J. Zehner, K. Nielsch, K. Leistner, *J. Mater. Chem. C* **2018**, *6*, 8411.
- [29] A. Quintana, E. Menéndez, M. O. Liedke, M. Butterling, A. Wagner, V. Sireus, P. Torruella, S. Estradé, F. Peiró, J. Dendooven, C. Detavernier, P. D. Murray, D. A. Gilbert, K. Liu, E. Pellicer, J. Nogués, *J. Sort. ACS Nano* **2018**, *12*, 10291.
- [30] X. Zhou, Y. Yan, M. Jiang, B. Cui, F. Pan, C. Song, *J. Phys. Chem. C* **2016**, *120*, 1633.
- [31] Q. Lu, B. Yildiz, *Nano Lett.* **2016**, *16*, 1186.
- [32] N. Lu, P. Zhang, Q. Zhang, R. Qiao, Q. He, H.-B. Li, Y. Wang, J. Guo, D. Zhang, Z. Duan, Z. Li, M. Wang, S. Yang, M. Yan, E. Arenholz, S. Zhou, W. Yang, L. Gu, C.-W. Nan, J. Wu, Y. Tokura, P. Yu, *Nature* **2017**, *546*, 124.
- [33] J. Walter, G. Yu, B. Yu, A. Grutter, B. Kirby, J. Borchers, Z. Zhang, H. Zhou, T. Birol, M. Greven, C. Leighton, *Phys. Rev. Mater.* **2017**, *1*, 071403.
- [34] H.-B. Li, N. Lu, Q. Zhang, Y. Wang, D. Feng, T. Chen, S. Yang, Z. Duan, Z. Li, Y. Shi, W. Wang, W.-H. Wang, K. Jin, H. Liu, J. Ma, L. Gu, C. Nan, P. Yu, *Nat. Commun.* **2017**, *8*, 2156.
- [35] M. Wang, X. Sui, Y. Wang, Y. Juan, Y. Lyu, H. Peng, T. Huang, S. Shen, C. Guo, J. Zhang, Z. Li, H. Li, N. Lu, A. T. N'Diaye, E. Arenholz, S. Zhou, Q. He, Y. Chu, W. Duan, P. Yu, *Adv. Mater.* **2019**, *31*, 1900458.
- [36] Y. N. Yan, X. J. Zhou, F. Li, B. Cui, Y. Y. Wang, G. Y. Wang, F. Pan, C. Song, *Appl. Phys. Lett.* **2015**, *107*, 122407.
- [37] M. Gößler, M. Albu, G. Klinser, E. Steyskal, H. Krenn, R. Würschum, *Small* **2019**, *15*, 1904523.
- [38] I. Koch, T. Granath, S. Hess, T. Ueltzhöffer, S. Deumel, C. I. Jauregui Caballero, A. Ehresmann, D. Holzinger, K. Mandel, *Adv. Opt. Mater.* **2018**, *6*, 1800133.
- [39] G. Lin, D. Makarov, O. G. Schmidt, *Lab Chip* **2017**, *17*, 1884.
- [40] X. Chen, X. Zhu, W. Xiao, G. Liu, Y. P. Feng, J. Ding, R.-W. Li, *ACS Nano* **2015**, *9*, 4210.
- [41] R. M. Cornell, U. Schwertmann, *The Iron Oxides: Structure, Properties, Reactions, Occurrences and Uses*, 1st ed., Wiley, New York **2003**.
- [42] Y. K. Kim, M. Oliveria, *J. Appl. Phys.* **1993**, *74*, 1233.
- [43] S. Meng, J. Wu, L. Zhao, H. Zheng, S. Jia, S. Hu, W. Meng, S. Pu, D. Zhao, J. Wang, *Chem. Mater.* **2018**, *30*, 7306.
- [44] N. B. Khojasteh, S. Apelt, U. Bergmann, S. Facsko, R. Heller, *Rev. Sci. Instrum.* **2019**, *90*, 085107.
- [45] T. G. Knorr, R. W. Hoffman, *Phys. Rev.* **1959**, *113*, 1039.
- [46] S. V. Komogortsev, S. N. Varnakov, S. A. Satsuk, I. A. Yakovlev, S. G. Ovchinnikov, *J. Magn. Magn. Mater.* **2014**, *351*, 104.
- [47] J. L. Bubendorff, S. Zabrocki, G. Garreau, S. Hajjar, R. Jaafar, D. Berling, A. Mehdaoui, C. Pirri, G. Gewinner, *Europhys. Lett.* **2006**, *75*, 119.

- [48] A. Barranco, A. Borrás, A. R. González-Elipé, A. Palmero, *Prog. Mater. Sci.* **2016**, 76, 59.
- [49] I. V. Soldatov, R. Schäfer, *J. Appl. Phys.* **2017**, 122, 153906.
- [50] E. C. Stoner, E. P. Wohlfarth, *Philos. Trans. R. Soc., A* **1948**, 240, 599.
- [51] A. Hubert, R. Schäfer, *Magnetic Domains*, Springer, Berlin **1998**.
- [52] E. Feldtkeller, *It – Inf. Technol.* **1961**, 3, 167.
- [53] J. Nowak, E. Szibel, *IEEE Trans. Magn.* **1984**, 20, 2105.
- [54] O. Idigoras, A. K. Suszka, P. Vavassori, P. Landeros, J. M. Porro, A. Berger, *Phys. Rev. B* **2011**, 84, 132403.
- [55] H. Hoffmann, *Phys. Status Solidi* **1964**, 5, 187.
- [56] K. J. Harte, *J. Appl. Phys.* **1968**, 39, 1503.
- [57] J. Steiner, R. Schäfer, H. Wiczorek, J. McCord, F. Otto, *Phys. Rev. B* **2012**, 85, 104407.
- [58] S. Mallick, S. Mallik, B. B. Singh, N. Chowdhury, R. Gieniusz, A. Maziewski, S. Bedanta, *J. Phys. D: Appl. Phys.* **2018**, 51, 275003.
- [59] K. Duschek, M. Uhlemann, H. Schlörb, K. Nielsch, K. Leistner, *Electrochem. Commun.* **2016**, 72, 153.
- [60] Z. He, R. V. Gudavarthy, J. A. Koza, J. A. Switzer, *J. Am. Chem. Soc.* **2011**, 133, 12358.
- [61] E. Lopatina, I. Soldatov, V. Budinsky, M. Marsilius, L. Schultz, G. Herzer, R. Schäfer, *Acta Mater.* **2015**, 96, 10.
- [62] T. Maruyama, Y. Shiota, T. Nozaki, K. Ohta, N. Toda, M. Mizuguchi, A. A. Tulapurkar, T. Shinjo, M. Shiraishi, S. Mizukami, Y. Ando, Y. Suzuki, *Nat. Nanotechnol.* **2009**, 4, 158.
- [63] U. Bauer, M. Przybylski, G. S. D. Beach, *Phys. Rev. B* **2014**, 89, 174402.
- [64] G. Herzer, *IEEE Trans. Magn.* **1990**, 26, 1397.
- [65] C.-H.-T. Chang, W.-H. Kuo, Y.-C. Chang, J.-S. Tsay, S.-L. Yau, *Sci. Rep.* **2017**, 7, 43700.
- [66] G. Q. Li, H. Takahoshi, H. Ito, H. Saito, S. Ishio, T. Shima, K. Takanashi, *J. Appl. Phys.* **2003**, 94, 5672.
- [67] T. G. Woodcock, Y. Zhang, G. Hrkac, G. Ciuta, N. M. Dempsey, T. Schrefl, O. Gutfleisch, D. Givord, *Scr. Mater.* **2012**, 67, 536.
- [68] D. A. Allwood, *Science* **2005**, 309, 1688.
- [69] F. Ando, H. Kakizakai, T. Koyama, K. Yamada, M. Kawaguchi, S. Kim, K.-J. Kim, T. Moriyama, D. Chiba, T. Ono, *Appl. Phys. Lett.* **2016**, 109, 022401.
- [70] C. Grezes, F. Ebrahimi, J. G. Alzate, X. Cai, J. A. Katine, J. Langer, B. Ocker, P. Khalili Amiri, K. L. Wang, *Appl. Phys. Lett.* **2016**, 108, 012403.
- [71] Z. Wang, H. Wu, G. W. Burr, C. S. Hwang, K. L. Wang, Q. Xia, J. J. Yang, *Nat. Rev. Mater.* **2020**, 5, 173.
- [72] G. Schiavone, M. Desmulliez, A. Walton, *Micromachines* **2014**, 5, 622.
- [73] O. Cugat, J. Delamare, G. Reyne, *IEEE Trans. Magn.* **2003**, 39, 3607.
- [74] M. Mayer, *AIP Conf. Proc.* **1999**, 475, 541.
- [75] M. Nichterwitz, S. Honnali, J. Zehner, S. Schneider, D. Pohl, S. Schiemenz, S. T. B. Goennenwein, K. Nielsch, K. Leistner, *ACS Appl. Electron. Mater.* **2020**, 2, 2543.
- [76] I. V. Soldatov, R. Schäfer, *Rev. Sci. Instrum.* **2017**, 88, 073701.